Biomimetic mineralization of hierarchical nanofiber shish-kebabs in a concentrated apatite-forming solution

Sarah E. Gleeson, † Seyong Kim, † Qian Qian, † Tony Yu, † Michele Marcolongo, † , †† Christopher Y. $Li^{\dagger*}$

[†]Department of Materials Science and Engineering, Drexel University, Philadelphia, PA 19104

††Department of Mechanical Engineering, Villanova University, Villanova, PA 19085

KEYWORDS: biomineralization, nanofiber, nanofiber shish-kebabs, bone, calcium phosphate

ABSTRACT: Recently, hierarchical polymer nanostructures called nanofiber shish-kebabs (NFSKs) have shown great potential in directing the distribution of minerals for biomineralization. In this work, we report controlled biomimetic mineralization in block copolymer-containing NFSKs. NFSKs were formed by crystallizing polycaprolactone-block-poly(acrylic acid) (PCL-b-PAA) kebabs on PCL fiber backbones. The block copolymer kebabs were periodically distributed on PCL nanofibers with a spacing of ~ 100 -300 nm. Free ions could infiltrate into anionic PAA nanodomains and initiate the NFSK-templated biomimetic mineralization process. A concentrated calcium phosphate solution was used in the present study, which led to significantly accelerated mineralization kinetics compared with the previously studied simulated body fluid systems. Electron microscopy, Fourier-transform infrared spectroscopy, and wide-angle X-ray diffraction were used to characterize the structure and morphology of the mineralized NFSKs. A three-stage mineralization process was identified, and carbonated non-stoichiometric hydroxyapatite was

observed after stage II with the mineral location templated within kebabs. This accelerated

mineralization process yielded a periodic mineral distribution of a biomimetic calcium phosphate

phase along the fibers, and the decrease in mineral formation time allows for more efficient

biomineralization study and composite formation.

Corresponding Author

*Prof. C.Y. Li, E-mail: chrisli@drexel.edu

1. Introduction

Each year, approximately 2.2 million bone graft procedures are performed worldwide, being

used in 20-25% of all bone and joint surgeries and 25% of all dental implants. 1-2 While bone

autografts have been the gold standard of treatment for decades, autografts are associated with

infection, sensory loss, hematoma, and longer hospital stays.³ For these reasons, the use of

synthetic bone substitutes is on the rise as a promising alternative for facilitating bone healing after

injury, cancer, or other disease. Electrospinning has emerged as a promising technique for bone

tissue engineering due to the similarity of electrospun nanofibers to the extracellular matrix.

Electrospun fibrous materials are advantageous as osteogenic substrates due to their high surface-

to-volume ratio, large interconnected pores with a tunable porosity, and surfaces that are easily

functionalized.⁴⁻⁶

To design electrospun scaffolds that more closely match the mechanical and osteogenic behavior

of natural bone, researchers have begun to take inspiration from bone's composite nanostructure.

In bone, the organic matrix is primarily comprised of tropocollagen molecules staggered along a

2

collagen fibril, creating gap zones ~40 nm in length with a period of 67 nm.⁷⁻⁸ The calcium phosphate bone mineral is a poorly crystalline, non-stoichiometric carbonated apatite which forms into platelet crystals within the gap zones, creating an intricate nanoscale interaction between collagen and mineral. In natural bone, mineral formation is guided by chemical and physical cues from the tissue, including charged functional groups and gap zones within collagen fibrils. The collagen matrix renders precise orientational and spatial control over the mineral nanocrystals, and recreating bone's complex nanostructure in a composite fibrous material is challenging.

There are two common routes for incorporating calcium phosphate mineral crystals in electrospun fibers: co-electrospinning a composite solution or biomineralization. Co-electrospinning involves combining a mineral phase with a polymer solution and electrospinning the two components directly into hybrid fibers. This technique has been shown to effectively mix nanocrystalline hydroxyapatite (HAP) with natural polymers, 9 synthetic polymers, 10, and blends. 11 Although the addition of co-electrospun mineral improves the biocompatibility, bioactivity, and mechanical properties of nanofibrous mats, only a limited amount of mineral can be incorporated without aggregation, and there is poor control over the distribution of minerals within the fiber. 11

Another method to incorporate mineral into electrospun fibers is through biomineralization, in which ions from the surrounding environment are assembled into bioinorganic crystals.¹² Fiber mats can be alternately dipped in calcium-containing and then phosphate-containing solutions to rapidly build up a mineral coating on the surface of synthetic,¹³ natural,¹⁴, or blend fibers.¹⁵ However, surface mineralization of nanofibers in solution often leads to randomly deposited HAP coatings rather than localized control and structure of the mineral.

Mineral orientation on nanofibers has been achieved using self-assembled peptides with charged phosphoserine residues¹⁶ and bile acid groups on polymer fibers.¹⁷ Natural polymer structures can

also be exploited to direct mineral growth, with improved biomimicry when mineral templating and sequestering molecules are utilized. Recommendatively, control over mineral spatial distribution can be achieved by using block copolymer (BCP) templates. BCPs are attractive materials for directing nanoscale mineralization due to their self-assembly into morphologies with high spatial resolution. Unique morphologies for a variety of inorganic minerals have been induced using BCP assemblies, including double hydrophilic BCP, Recommendation and confinement within domains of Pluronic triblock copolymers. Song et al. incorporated amorphous calcium phosphate nanoparticles into BCP hydrophilic domains, leading to different self-assembled structures of mineral with nanoscale resolution.

In order to take advantage of the biocompatibility of electrospun fibers as well as the nanoscale domain resolution of BCP, these nanoarchitectures were recently combined into a single hierarchical material called a nanofiber shish-kebab (NFSK).²⁷⁻³⁰ NFSKs were comprised of an electrospun polymer backbone "shish" with polymers crystallized periodically onto the surface in a repeating homopolymer or BCP "kebab" structure.³¹⁻³³ The formation of this unique nanostructure was attributed to the size-dependent soft epitaxy mechanism.^{29, 34-35} NFSK composites were created via mineral-nucleating functionalities that have been incorporated into NFSKs using co-electrospun HAP nanocrystals or chitosan within kebabs. However, these methods resulted in undirected mineral growth on the NFSK surface when incubated in 2x concentrated simulated body fluid (SBF).³⁶⁻³⁷ For better control over mineral formation, Chen *et al.* used polycaprolactone-*block*-poly (acrylic acid) (PCL-*b*-PAA) as the kebab-forming polymer, resulting in lamellar domains as PCL crystallizes and excludes PAA to the crystal surface.²⁸ The anionic PAA domains then recruited and confined mineral ions from solution, as seen in **Figure**

1. After mineralizing for 5 days in 2xSBF, they found crystalline calcium phosphate mineral within the kebabs, with the kebab spacing controlling the periodic distribution of mineral along the fibers.

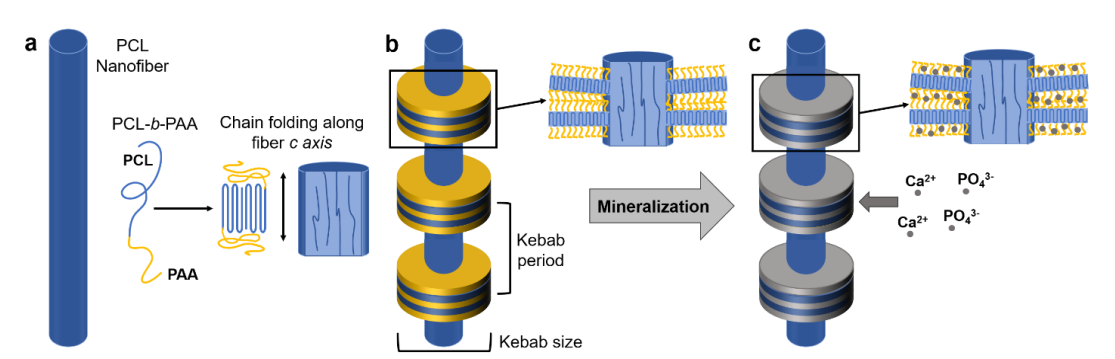


Figure 1. Schematic of formation and mineralization of NFSKs. a) PCL-*b*-PAA block copolymers in dilute solution crystallized with PCL chains aligned with the PCL nanofibers. b) NFSKs have periodically spaced kebabs along the fiber backbone, with each kebab containing PCL (blue) and PAA (yellow) lamellae. c) When incubated in a solution containing calcium and phosphate ions, the negatively charged PAA domains recruit calcium ions, leading to mineral formation confined within the PAA regions.

Previous NFSK studies have focused on biomineralization using 2xSBF, which yields bone-like carbonated hydroxyapatite (cHAP) phases but is a slow process over several days. The often-used SBF includes other biologically occurring ions in similar concentrations as found in the body, which slows down the mineralization process.³⁸ Mg²⁺ and HCO₃⁻ ions in SBF have been found to have an inhibitory effect on calcium phosphate crystal growth, and supersaturated solutions that exclude these species demonstrate faster mineral precipitation.³⁹⁻⁴⁰ Faster mineralization kinetics are desirable for mechanistic studies on nanoconfined mineralization. The aim of the present study is to accelerate the controlled mineralization of NFSKs. NFSKs with PCL-*b*-PAA kebabs were

selected for their ability to induce and direct mineral formation from a concentrated calcium phosphate salt solution. To speed up mineralization, a solution with a higher concentration of HAP-forming ions was used, which was shown to lead to faster calcium phosphate formation.⁴¹ Our results showed that controlled mineralization occurs in the ~10nm thin BCP galleries that are periodically located along polymer nanofibers. Since changes to the mineralization solution have been shown to impact the formation of the calcium phosphate phase,^{40, 42-43} the biomimicry of the mineral phase during this accelerated process was evaluated. Three stages of mineralization were identified, and the bone mimicking cHAP was formed within 8 hrs.

2. Materials and Methods

2.1 Materials.

ε-caprolactone (ε-CL, 97%), tin(II) 2-ethylhexanoate (Sn(Oct)₂, 92.5-100.0%), 2,2'-Azobis(2-methylpropionitrile) (AIBN, 98%), *tert*-butyl acrylate (*t*BA, contains 10-20 ppm monomethyl ether hydroquinone inhibitor, 98%), trifluoroacetic acid (TFA, reagent grade, 99%), PCL (M_n 80,000 g/mol), 2,2,2-trifluoroethanol (TFE, reagent grade, ≥99%), pentyl acetate (PA, ≥99%, food grade), calcium chloride dihydrate (CaCl₂•2H₂O, ACS reagent, ≥99%), and potassium phosphate dibasic (K₂HPO₄, ACS reagent, ≥99%) were purchased from Sigma-Aldrich (St. Louis, MO, USA). Ethanol (EtOH, ACS Reagent, ≥99.5%), and 10X tris-buffered saline (TBS, pH 7.4) were purchased from VWR (Radnor, PA, USA). PA was distilled over calcium hydride, *t*BA was passed twice through basic aluminum oxide columns to remove the inhibitor, and all other chemicals were used as received.

2.2 Synthesis of PCL-b-PAA.

PCL-*b*-PAA was synthesized by ring-opening polymerization (ROP) and reversible addition-fragmentation chain transfer (RAFT) polymerization as described in a previous report, and the full synthesis materials and methods can be found in the supporting information.²⁹ Briefly, the BCP was synthesized in a three-step process. A dual ring-opening/RAFT agent was synthesized as reported by Petzetakis *et al.* with an alcohol end to facilitate ROP of ε-CL and a thiocarbonylthio chain transfer agent end for RAFT polymerization of *tert*-butyl acrylate (*t*BA) monomers.⁴⁴ The PCL-RAFT agent was synthesized via ROP, with Sn(Oct)2 serving as the catalyst for the reaction. Next, RAFT polymerization was used to create a poly (*tert*-butyl acrylate) (P*t*BA) block, forming PCL-*b*-P*t*BA. AIBN was used as the radical initiator for the RAFT reaction. Finally, the *tert*-butyl groups were hydrolyzed with TFA to form PCL-*b*-PAA. All structures and molecular weights were determined with proton nuclear magnetic resonance spectroscopy (¹H NMR) and gel permeation chromatography (GPC) (**Figure S1, Table S1**). The synthesized BCP was determined to be PCL₁₇₁-*b*-PAA₉₂ with 171 and 92 as the PCL and PAA degrees of polymerization, respectively.

2.3 Formation of NFSKs with PCL-b-PAA kebabs.

10 w/v% PCL in TFE was prepared by mixing with a magnetic stir bar at room temperature for at least 12 hr. A horizontal setup was used to electrospin PCL solutions onto a cylindrical grounded collector wrapped in aluminum foil. A high voltage power supply (Gamma High Voltage Research, Ormond Beach, FL, USA) applied a +18kV voltage to a blunt 1-inch 20-gauge needle. A syringe pump (KD Scientific, Holliston, MA, USA) kept a consistent polymer solution flow rate of 0.5 mL/h through the charged needle from a 5mL syringe. PCL fibers were collected for four hr at room temperature and a collection distance of 18cm. The fiber mats were dried overnight under vacuum.

NFSKs were made by crystallizing PCL-*b*-PAA onto the surface of electrospun nanofibers. Briefly, a 1:1 ratio of PA:EtOH was used as the solvent for a 1 w/v% solution of PCL-*b*-PAA. The BCP was dissolved at 70°C, then cooled to room temperature and 1 mL was added to a 1.5 cm x 1.5 cm square of PCL nanofibers in a glass vial. The fibers incubated in the stable room temperature solution for 0.5-10 min, and then were removed and rinsed three times with a room temperature mixture of 1:1 PA: EtOH. The NFSK mat was dried in a fume hood for 20 min, then under vacuum overnight.

2.4 Mineralization of NFSKs.

1X TBS was prepared by diluting 10X TBS buffer with deionized water. For studies testing different salt concentrations, the mineralization solutions were made by mixing a stock solution of 20mM CaCl₂•2H₂O in TBS with pure 1X TBS, followed by the addition of 8mM K₂HPO₄ in different ratios to reach the desired salt ion concentrations of 5 mM Ca²⁺/2 mM HPO₄²⁻, 6 mM Ca²⁺/2.4 mM HPO₄²⁻, and 7 mM Ca²⁺/2.8 mM HPO₄²⁻.

Further mineralization studies were performed in solutions of 6mM CaCl₂•2H₂O in TBS and 2.4mM K₂HPO₄ in TBS at pH 7.4. The mineralization solution was prepared by mixing separately prepared 14mL 8.57mM CaCl₂•2H₂O in TBS and 6mL 8mM K₂HPO₄ in TBS. The total ion concentrations for the solution and comparisons with 2xSBF and blood plasma are listed in **Table S2**. NFSKs were mineralized by incubating a 1.5 cm x 1.5 cm NFSK mat in the mineralization solution at room temperature, with gentle 100 rpm shaking for the first 2 hr. When samples were removed from the mineralization solution, they were rinsed three times with deionized water and dried under vacuum overnight.

2.5 Characterization.

Scanning electron microscope (SEM) images were taken using a Zeiss Supra 50VP microscope at an accelerating voltage of 1 kV. Before imaging, SEM samples were coated with 80/20 Pt/Pd for 30 s with a Cressington 208HR sputter coater. ImageJ software was used to take measurements of NFSK dimensions from SEM images, with at least 25 kebab diameter measurements and 15 kebab period measurements (averaged over 4 adjacent kebabs) made for each incubation time. Energy dispersive X-ray spectrometry (EDS) was performed on uncoated samples at 8.5 kV accelerating voltage with detection using an Oxford AztecOne system attached to a Zeiss Supra 50VP SEM. Transmission electron microscopy (TEM) samples were prepared by finely cutting mineralized NFSK mats into small pieces, then dispersing in EtOH and sonicating with a probe sonicator for 5 min. EtOH-NFSK suspension was drop-cast onto carbon-coated copper TEM grids, and unstained images were taken on a JEOL JEM2100 using an accelerating voltage of 120 keV. Attenuated total reflection Fourier-transform infrared spectroscopy (ATR-FTIR) measurements were performed using a Thermo Nicolet Nexus 870 Spectrometer with 32 scans performed for each sample at a 4 cm⁻¹ resolution. Wide-angle X-ray diffraction (WAXD) was taken using a Rigaku S-MAX 3000 with a copper target operated at 45kV/0.88mA to generate X-rays, and a silicon standard was used to calibrate the 2D diffraction pattern. Saxsgui software was used to convert 2D WAXD patterns into 1D plots.

3. Results and Discussion

3.1 Effect of incubation time on kebab dimensions.

It has been previously demonstrated that for PCL kebabs the kebab size and period increase as incubation time increases.^{32, 45} However, BCP crystal growth could be quite different from PCL homopolymer, and desired crystalline morphology can only be formed when crystallization instead

of BCP phase separation dominates the structure formation process. 46-48 For PCL-b-PAA BCP kebabs, incubation times ranging from 0.5 min to 10 min were tested for their effect on NFSK morphology, as seen in **Figure 2**. PCL electrospun nanofibers had an average diameter of 351 ± 177 nm (**Figure 2a**). After 0.5 min incubation in a dilute solution of PCL-b-PAA, small kebab crystals were seen densely nucleated on the fibers (**Figure 2b**). Within 2 min, the small crystals grew into well-defined toroidal kebabs on the PCL nanofiber surface (**Figure 2c**). As incubation time increased, the kebabs grew larger and the distance between adjacent kebabs increased. **Figure 2e** shows an image of kebabs grown for 10 min incubation, where the kebab crystals converge along both the fiber axis and the orthogonal direction. The partial collapse of the kebab crystal edges led to the warping of the kebabs (highlighted with red arrows). On the other hand, kebabs formed on locally aligned fibers are parallel to each other and merged into one larger lamella (blue arrows).

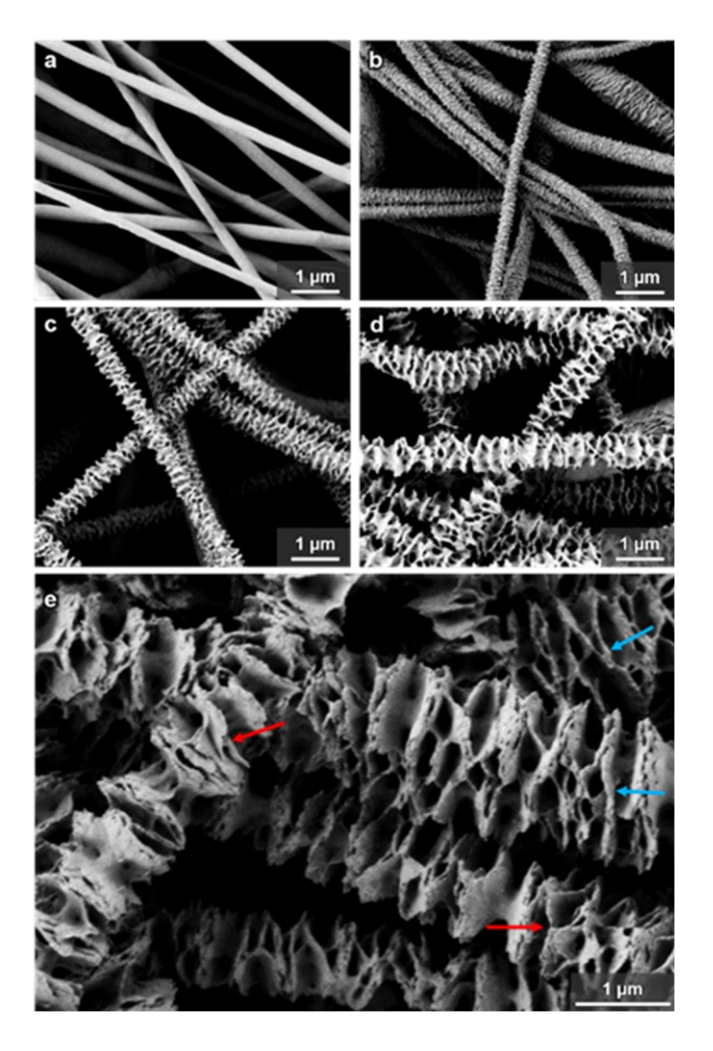


Figure 2. SEM images of a) PCL electrospun nanofibers, as well as NFSK formed by incubation for b) 0.5 min, c) 2 min, d) 5 min, e) 10 min. The 10 min incubation in panel e is expanded to show details of the merging adjacent kebabs along a single NFSK (indicated with red arrows) as well as the merged kebabs from adjacent and parallel fibers (blue arrows).

The kebab dimensions at each incubation time were measured and plotted in **Figure 3**. Kebab size and period both increased with incubation time, indicating that the merging of adjacent kebabs continued as the kebab crystals increased in lateral dimension. Kebab size increased over time due to more polymer chains diffusing to the kebab growth front at the toroid edge, growing the crystal

laterally from the fiber. Due to the variability of PCL shish diameters, lateral crystal growth was difficult to determine and therefore kebab size was considered to be the average outer diameter of the toroids. For toroidal crystals formed after 2 min incubation, the average kebab size was 518 ± 59 nm, and almost doubled in diameter after 10 min. Kebab period increased from 165 ± 22 nm to 304 ± 66 nm over the same time frame. Kebab period likely increased with incubation time due to kebabs being drawn together by elasto-capillary force, which was observed to induce the collapse of flat and spherical polymer crystals. $^{49-51}$ As kebabs grew, the interfacial energy between kebabs and the poor solvent could overcome the bending rigidity of the plate-like crystals, leading to adjacent kebabs merging as they increase in size. 49 10 min incubation time was selected for NFSK mineralization in order to have large kebabs for studying mineral formation.

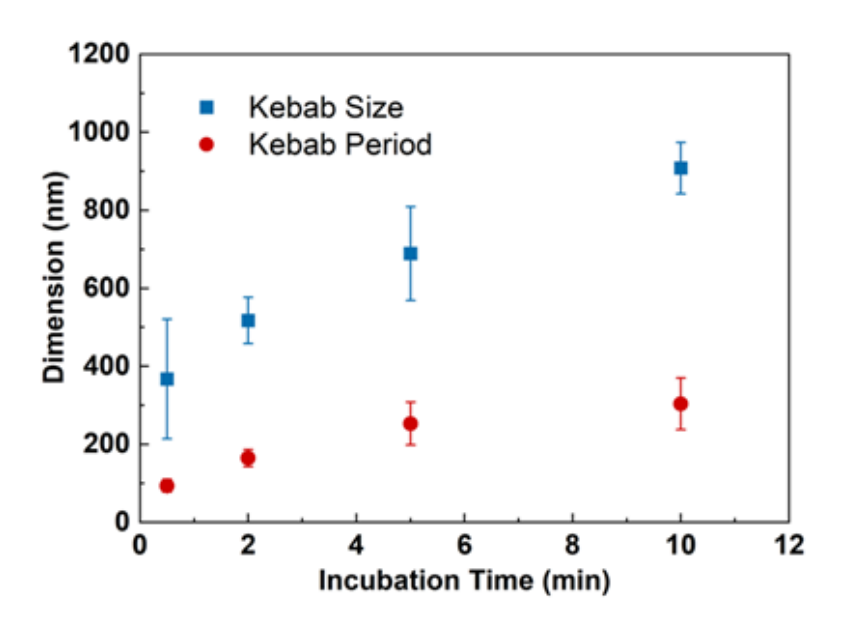


Figure 3. Plot of kebab size and period as a function of incubation time in dilute PCL-*b*-PAA solution.

3.2 Mineralization in concentrated solution.

All NFSK samples for mineralization studies were prepared via 10 min incubation time of PCL-b-PAA. The NFSK samples were mineralized by incubating in a concentrated salt solution containing calcium and phosphate ions. Different concentrations of calcium and phosphate salts in buffered solution were tested to determine the impact on NFSK mineralization. As the salt concentrations were increased, a greater amount of surface mineral was seen at the same time points under FTIR and SEM in **Figure S2**. For in-depth study of the mineralization process in these apatite-forming solutions, 6mM Ca²⁺/2.4mM HPO₄²⁻ salt concentrations were selected so as to yield faster mineralization kinetics without rapid mineral precipitation from solution.

NFSKs were mineralized in a concentrated calcium phosphate solution for up to 12 hr, with samples taken every few hours for characterization. SEM images of the mineralized NFSK mats can be seen in **Figure 4**. There was little morphological change in the NFSK mat over the first 8 hr of mineralization, other than a roughening of the kebab edge that was initially observed after 2 hr (**Figure 4b**). Low magnification SEM images confirm that the NFSK mat is free of visible morphological changes across the mat surface over 8 hr mineralization time (**Figure S3**). No minerals were seen outside of the kebabs until 12 hr mineralizing, when the NFSK mat surface was covered with a network of mineral overgrowth. **Figure 4f** shows a NFSK surrounded by overgrown mineral, and the mineral was seen extending from the edges of kebab crystals to fill in the pores of the NFSK mat. **Figure 5a** is a low magnification image of a NFSK mat surface with mineral overgrowth after 12 hr. Interestingly, minerals were filling in the extrafibrillar space across the entire surface of the NFSK mat.

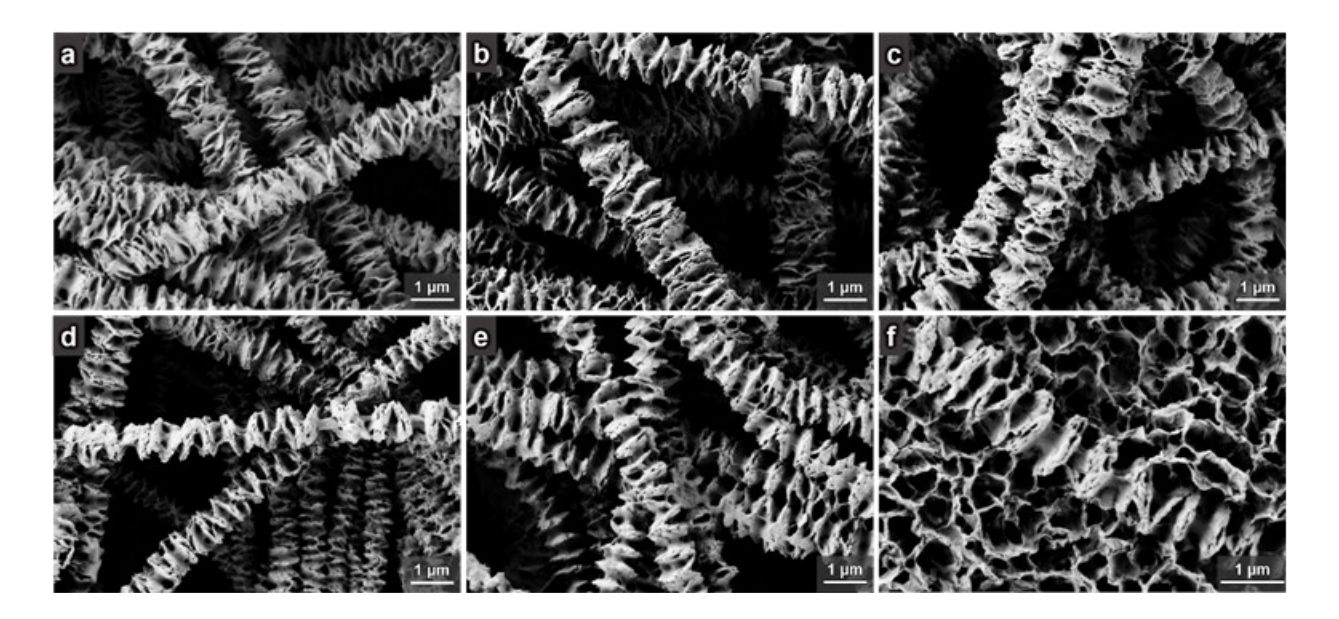


Figure 4. SEM images of a) non-mineralized NFSK, and NFSK mineralized for b) 2 hr, c) 4 hr, d) 6 hr, e) 8 hr, f) 12 hr.

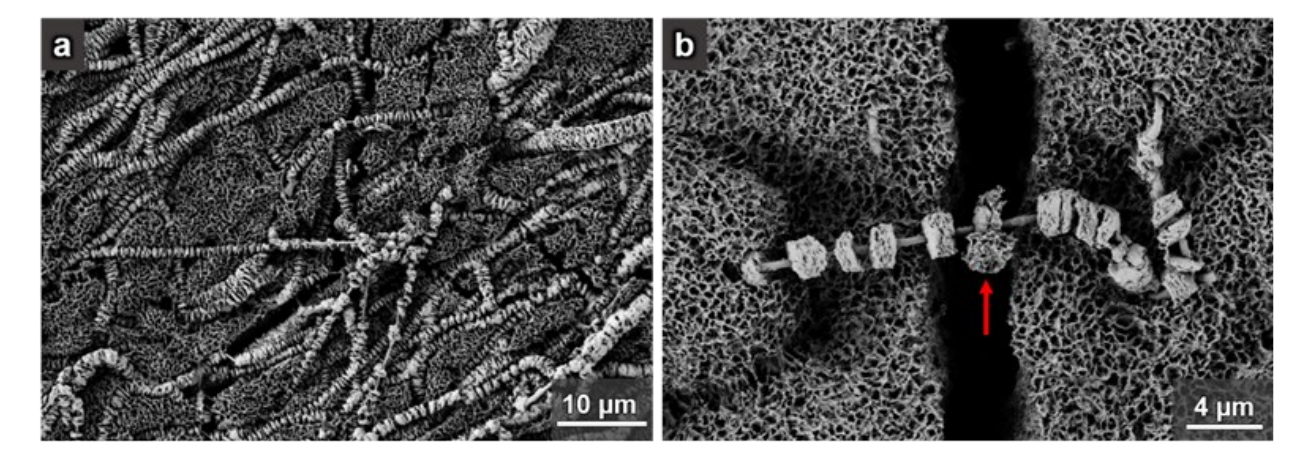


Figure 5. SEM images of NFSKs mineralized for 12 hr. a) Low-magnification image showing how overgrown mineral fills in the spaces between fibers, eventually growing outwards from the mat surface and completely obscuring the NFSK morphology. b) An individual NFSK fiber that spanned a gap in the mineral coating, showing how an "isolated" kebab such as the one indicated by the red arrow can have mineral growing outwards from its surface.

Figure 4f and Figure 5b show minerals connecting directly to individual kebab edges and growing outwards from kebabs isolated from the overgrown mineral. The mineral overgrowth likely begins with the mineralized kebabs serving as the nucleation site for deposits of new mineral to grow outwards from the structure. Due to the highly supersaturated nature of the mineralizing solution, repeated experiments showed that this overgrowth would occur over a range of times which could be as short as 10 hr, or extend past 12 hr such that 12 hr samples would not always show visible mineral. Figure S4 shows an SEM image of 10 hr mineralized NFSK mat which resembles the 8 hr sample in Figure 4e and does not have overgrown mineral in the extrafibrillar space. However, less commonly the 10 hr time point could result in excessive surface mineral. This variance in mineral content beyond 8 hr is likely due to slight variations in kebab size and the rapid progression of mineral overgrowth once it has extended outside of the kebab domains. We therefore consider the overgrowth stage to occur in a wide window of times beyond 8 hr.

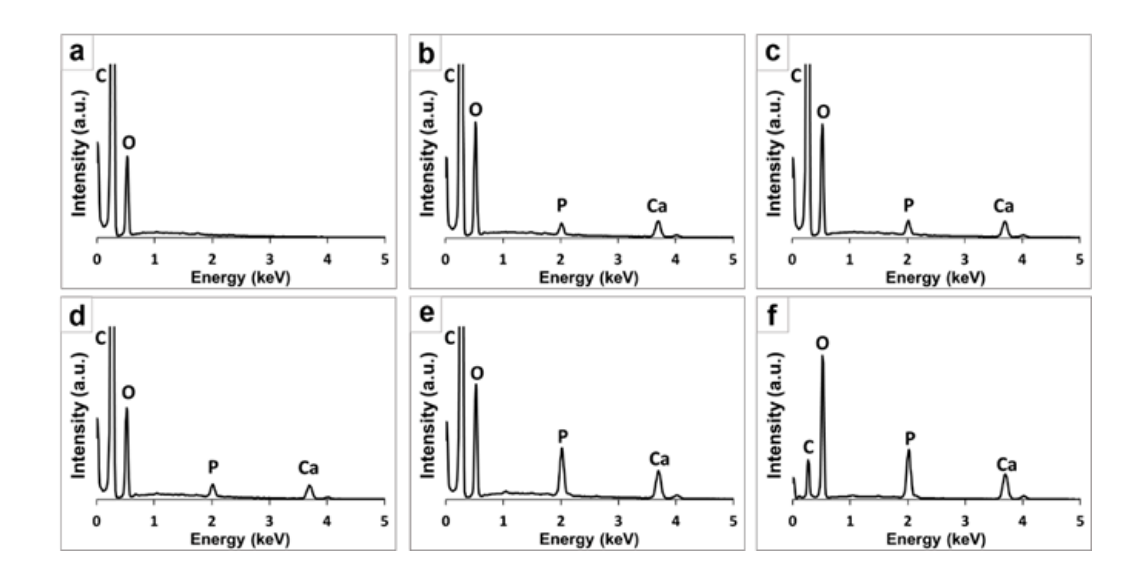


Figure 6. EDS spectra showing the elements present on the surface of a) non-mineralized NFSK, and NFSK mineralized for b) 2 hr, c) 4 hr, d) 6 hr, e) 8 hr, f) 12 hr.

The presence of calcium and phosphorous elements on the surface of mineralized NFSKs were confirmed by EDS (Figure 6, Figure S5). Non-mineralized NFSKs showed peaks corresponding to carbon and oxygen (Figure 6a), which can be found in the PCL and PAA components of NFSKs. After being mineralized for only 2 hours, calcium and phosphorous were detected in low quantities on the mat surface (Figure 6b). From 2-8 hr mineralization, Ca and P EDS signals remained relatively constant. For the excessively mineralized 12 hr sample in Figure 6f, EDS showed more significant calcium and phosphorous content, as well as a carbon peak with much lower intensity. Due to EDS being a surface characterization technique, as the surface mineral layer builds up, the spectral analysis was detecting Ca, P, and O from the minerals along with a reduced fraction of C from the polymer substrate. Although EDS revealed that mineral ions entered the NFSK structure rapidly within 2 hr, a significant increase was not seen in the content of relevant mineral elements until overgrowth from kebabs occurred.

EDS showed that calcium and phosphorous elements were present in the NFSK mat across all mineralization times, thus TEM imaging was employed to determine the location of the mineral ions. NFSKs mineralized for 6 hr were dispersed by sonicating in ethanol and then cast onto carbon-coated copper grids so as to isolate individual NFSKs for TEM. **Figures 7a,b** show TEM images of a 6 hr mineralized kebab. Distinct striations were seen in the kebab, with the light kebab areas indicating PCL crystals, while the dark stripes showed that electron-dense mineral ions had entered the PAA layers. The mineral appeared to have penetrated several hundred nm into the kebabs, indicating that ions were able to diffuse through the PAA regions as minerals were found throughout the kebab rather than just near the single crystal surface. These images therefore demonstrate the overall morphology of the mineralized fiber at an early stage and suggest that

infiltrated ions facilitated the initiation of mineralization. The TEM images in Figure 7a,b show that there were approximately 7-12 layers of PCL/PAA alternating lamellae per kebab aggregation, while kebabs ranging from 6 to over 20 layers were observed elsewhere in the sample (as seen in the supporting information Figure S6). The presence of kebabs with large number of PCL/PAA layers can be attributed to the merging of smaller kebabs. In Figure 7b, the BCP lamellae are perpendicular to the fiber surface near the kebab edge, but as they approach the fiber surface these domains bend until almost parallel to the fiber axis. This supports the proposed mechanism of kebab period increasing with incubation time: while kebabs may have separately nucleated along the fiber, as they grow larger, they begin to bend and merge together (shown in Figure 2e). This merging can be seen in SEM images of the sonicated and drop-cast 6 hr mineralized NFSK (Figure 7c), where individual kebabs can be seen to be made up of many lamellae similar to the unmineralized NFSK in Figure 2e. Adjacent kebabs may be considered as parallel free-fixed plates so that as they increase in size and exceed the elasto-capillary length, they collapse upon solvent evaporation.^{29, 35, 49} As diagrammed in **Figure 7d**, kebabs with fewer layers will have less bending rigidity, and when the kebab diameter reaches a critical value, the crystal will bend to merge with the nearest adjacent kebab, resulting in warping of the PCL/PAA lamellar domains.

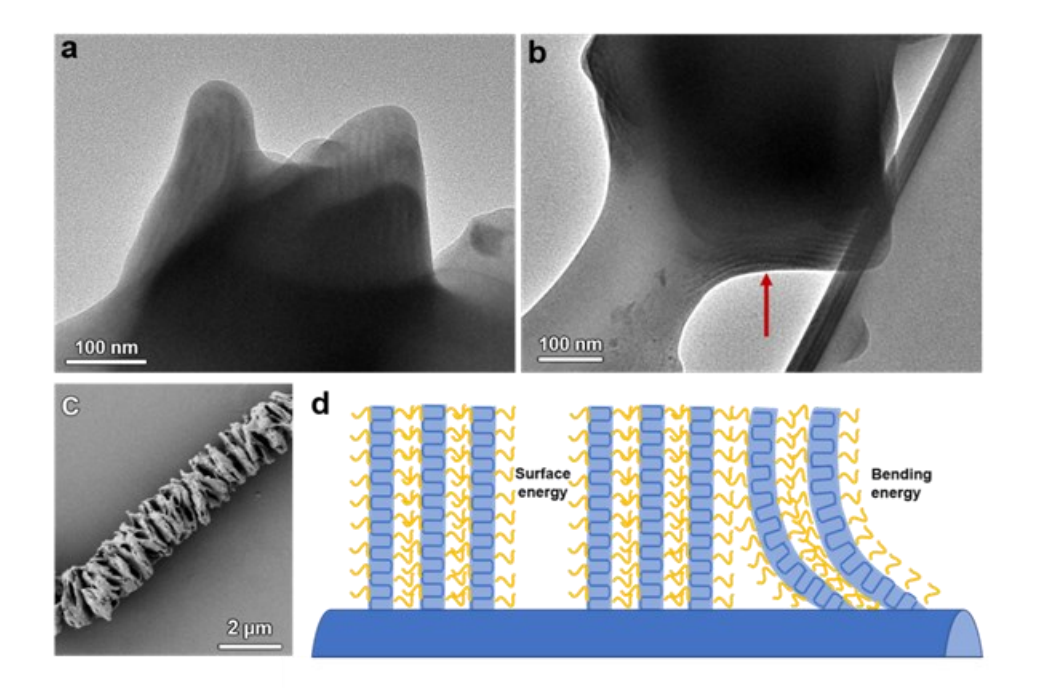


Figure 7. a) TEM image of NFSKs mineralized for 6 hr. Dark stripes within kebabs show regions where mineral ions lead to enhanced contrast. b) TEM image showing the bending of kebab lamellae near the fiber surface for a 6 hr mineralized sample. The bending onset is indicated with an arrow. c) SEM image showing kebab merging in NFSKs mineralized for 6 hr. d) Schematic showing the proposed mechanism of kebab bending and merging to reduce surface energy.

3.3 Evolution of mineral phases.

The ATR-FTIR spectra for each time point of NFSK mineralization can be seen in **Figure 8a**. Peak assignments for the full FTIR spectra can be found in **Table S3** of the supporting information. Within 2 hr mineralizing, a peak appeared at 1563 cm⁻¹ corresponding to the carbonate chemical group, but no evidence of phosphate was observed. By four hr, there were two slight peaks forming at 1013 cm⁻¹ and 556 cm⁻¹, indicating the detection of the v₃(PO₄) and v₄(PO₄) bands, respectively. As mineralization time increases, a second characteristic peak of v₄(PO₄) can be seen at 598 cm⁻¹. The intensity of all phosphate peaks relative to the PCL peaks increased with each subsequent time

point as the amount of mineral increased in the NFSKs, and at 12 hr the phosphate peaks have dwarfed the NFSK peaks.

The FTIR spectra was analyzed to determine the calcium phosphate phase formed during NFSK mineralization from concentrated solution. In the 12-hour spectrum, a v₁(PO₄) peak was seen at 962 cm⁻¹, which is typical for HAP, octacalcium phosphate (OCP), or nanocrystalline cHAP samples. No peaks were seen in any mineralized NFSK at 632 cm⁻¹ or 3572 cm⁻¹, which could be the result of low crystallinity in the mineral phase or a reduced presence of OH- groups, both of which indicate a nanocrystalline cHAP phase rather than HAP.⁵² Figure 8a shows a highwavenumber shoulder on the broad v₃(PO₄) peak and a low-wavenumber shoulder on the v₄(PO₄) peaks due to the presence of HPO₄²⁻ ions which are not found in stoichiometric HAP. Therefore, it is unlikely that HAP was the dominant calcium phosphate phase present. OCP was also not a significant mineral phase in the NFSKs. The high-wavenumber shoulder on the v₃(PO₄) peak was broad and smooth, typical of dried cHAP, while for OCP this shoulder would be expected to be more defined and comprised of distinct peaks due to higher crystallinity.⁵² Although at shorter time points the peak intensity was lower, the breadth of the v₃(PO₄) band and the presence of carbonate ions suggested that a poorly crystalline cHAP phase was present. These spectral clues were most evident at 12 hr when the mineral was overgrown, yet the same mineral phase was believed to be found confined within kebabs due to the presence of carbonate and water peaks (shown in the extended wavenumber FTIR plot in **Figure S7**) at 6 and 8 hours, which were less significant for OCP and HAP respectively. Therefore, the FTIR results indicated that the calcium phosphate phase present was a carbonated non-stoichiometric cHAP, which is similar to the mineral found in natural bone.

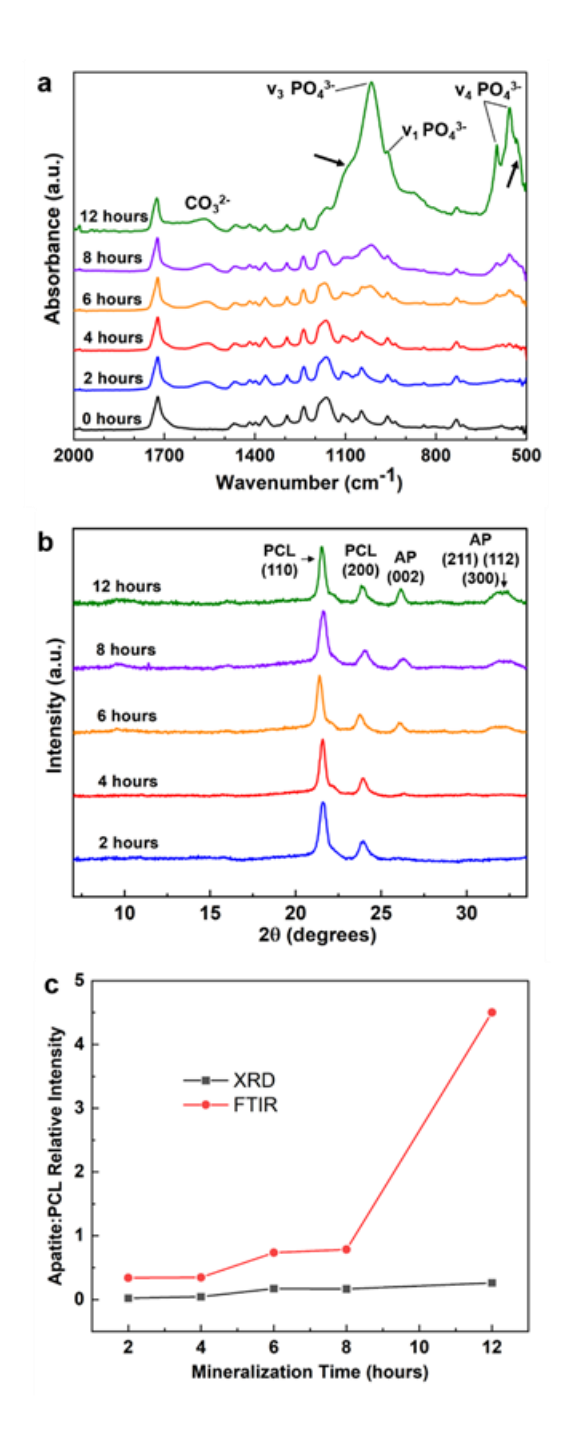


Figure 8. a) ATR-FTIR spectra of a non-mineralized NFSK mat and NFSKs mineralized for 2-12 hr. The arrows indicate peak shoulders corresponding to the presence of HPO₄²⁻ ions. b) WAXD plots of mineralized NFSKs. c) Plot of mineral peak intensity relative to PCL in NFSKs over time as quantified from WAXD and FTIR. WAXD relative intensity was quantified as hydroxyapatite

(002) plane peak intensity normalized to the PCL (110) peak. FTIR relative intensity was quantified as v₃(PO₄) maximum at 1013 cm⁻¹ normalized to PCL C=O stretching peak at 1720 cm⁻¹. The significant increase of the cHAP/PCL intensity at 12 hr for the FTIR sample was attributed to the surface overgrowth of mineral.

The crystal structure of the mineralized NFSKs was also studied using WAXD, as seen in **Figure 8b**. Two peaks were seen for all NFSK samples at 21.4° and 23.8° that correspond to the (110) and (200) planes of PCL, respectively. After mineralizing for 4 hr, a small peak was seen at 26.1°, which corresponds to the (002) planes in cHAP. This (002) cHAP peak appeared at the same time point in which a small phosphate peak was detected in the FTIR spectra. Starting at 6 hr, a broad peak encompassing the (211), (112), and (300) planes of cHAP formed around 32°, which is typical of nonstoichiometric cHAP or OCP. Therefore, the WAXD results confirmed that poorly crystalline cHAP was likely to be the mineral phase present in NFSK kebabs.

The relative amount of mineral was quantified and plotted as a function of mineralization time in **Figure 8c**. Note that the cHAP to PCL relative peak intensity in WAXD quantifies the amount of crystalline mineral present throughout the entire NFSK mat thickness, while ATR-FTIR data measures only a few µm deep from the surface. During the first 2 hr of mineralization, there was little evidence of cHAP crystals in NFSKs. There was a slight increase in mineral peak intensity at 4 hr, and a larger increase at 6 hr in both FTIR and WAXD data. The mineral peak intensity monitored by WAXD and FTIR increased slowly until the overgrowth stage at 12 hr mineralization. This overgrowth occurred predominantly on the surface of the NFSK mats and did not penetrate throughout, evidenced by the FTIR relative intensity in **Figure 8c** increasing by over 400% compared to a 50% increase in WAXD between 8 hr and 12 hr. This may occur due to the

limited accessibility of mineral-forming ions deep in the mat as diffusion is blocked by NFSKs and then by overgrown surface mineral filling in extrafibrillar pores.

Based on morphological, chemical, and structural information about the mineralized NFSK mats, NFSK-directed mineralization in the present study can be divided into three stages. In the first stage of mineralization, ions infiltrated into the PAA domains within kebabs, drawn in by electrostatic attraction between calcium ions and ionized carboxylic acid groups. This was confirmed by EDS results showing mineral elements present after two hours within the NFSK structure. In the second stage, the mineral ions undergo a phase transformation within the kebabs and began to crystallize, evidenced by the growing intensity of cHAP crystal peaks in WAXD and phosphate peaks in FTIR. Finally, in stage three, SEM confirmed that mineral grew out from the kebabs and filled the interstitial NFSK space. Since this growth was no longer confined by the PAA domains, it did not follow the biomimetic periodicity or orientation offered by the NFSK structure. This three-stage mechanism is shown in Figure 9.

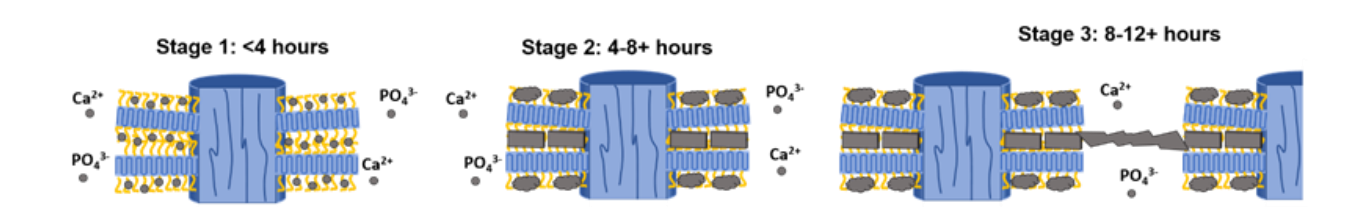


Figure 9. Stages of NFSK mineral formation. In stage 1, ions infiltrated into PAA domains but do not crystallize. Stage 2 is characterized by the transformation of amorphous mineral ions into crystalline mineral, but still confined within kebabs. Stage 3 occurs when mineral growth extends beyond the kebabs and begins to fill NFSK pores and bridge to adjacent fibers.

A similar mineralization mechanism was seen when NFSKs were mineralized in 2xSBF.²⁸ However, in 2xSBF the crystalline mineral took 3-5 days to form and overgrowth was only observed beyond 5 days, which is more than ten times slower than mineralization in concentrated calcium phosphate solution. After 7 days mineralizing, the NFSKs in 2xSBF had lost their shishkebab morphology as high mineral content led to overgrowth from kebabs, a stage reached in the concentrated ion solution at present in less than 12 hr. Other studies performed with NFSKs in 2xSBF similarly showed mineral forming over the course of several days, although details were not reported about the onset and development of mineral. 36-37 More recently, Chen et al. have performed NFSK mineralization in α-MEM cell culture medium which was found to significantly delay mineralization upwards of two weeks, likely due to the lower ion concentration and the mineral-inhibiting effect of the added protein serum in the medium.²⁷ The more rapid mineral formation reported at present is likely the combination of several factors. First, higher concentrations of mineral-forming ions were used, increasing both the Ca²⁺ and PO₄³⁻ molarity by 20%. Additionally, 2xSBF contains additional ions that are not present in the current study including Mg²⁺ and HCO₃⁻ which have been shown to have an inhibitory effect on mineralization. Therefore, these effects collectively accelerate the mineral formation process in the mineralization solution used in this work.

4. Conclusions

NFSK-directed biomimetic mineralization has successfully been achieved in a high concentration cHAP-forming solution, and the mineralization kinetics have been significantly accelerated – mineralization occurred in less than 12 hours while maintaining biomimicry of the resulting composites. During NFSK formation, kebab size was nearly doubled by increasing the

incubation time, and the merging of adjacent kebabs was shown. When incubated in the concentrated mineral ion solution, the PAA regions in the kebabs recruited mineral to preferentially form within 2D kebab domains first, with a three-stage mineral formation mechanism occurring as minerals accumulated, crystallized, and extended beyond the kebabs. The mineral closely matches what is expected from biological cHAP, confirming that the mineralized NFSKs are biomimetic in both composite nanostructure and mineral phase. This accelerated NFSK mineralization opens the door for rapid model study of composite mineralization, as well as for studying mineral inhibitors such as proteins or polyelectrolytes within a reasonable experimental time frame.

AUTHOR INFORMATION

Author Contributions. The manuscript was written through the contributions of all authors. All authors have given approval to the final version of the manuscript.

Acknowledgment. This work was partially supported by the National Science Foundation grant DMR-1507760, CMMI 1762626, the National Science Foundation Graduate Research Fellowship under Grant No. 1646737, the Department of Education Graduate Assistance in Areas of National Need (for S. Gleeson), and Drexel Dare grant. The authors would like to thank the students of Dr. Andrew Magenau's laboratory at Drexel University for their assistance with GPC data collection.

Abbreviations. PCL, polycaprolactone; PAA, poly(acrylic acid); NFSK, nanofiber shish-kebab; BCP, block copolymer; SBF, simulated body fluid; ROP, ring-opening polymerization; RAFT,

reversable addition-fragmentation chain transfer; cHAP, carbonated hydroxyapatite; HAP, hydroxyapatite; OCP, octacalcium phosphate; SEM, scanning electron microscope; EDS, Energy dispersive X-ray spectrometry; TEM, transmission electron microscope; ATR-FTIR, attenuated total reflection Fourier-transform infrared spectroscopy; WAXD, wide-angle X-ray diffraction.

Supporting Information. PDF file including detailed synthesis information, supplemental characterization figures, FTIR peak assignments, ion concentrations in solution

References

- 1. Deev, R. V.; Drobyshev, A. Y.; Bozo, I. Y.; Isaev, A. A., Ordinary and activated bone grafts: Applied classification and the main features. *BioMed Research International* **2015**, *2015*, 365050.
- 2. Calori, G. M.; Mazza, E.; Colombo, M.; Ripamonti, C., The use of bone-graft substitutes in large bone defects: any specific needs? *Injury* **2011**, *42 Suppl 2*, S56-63.
- 3. Younger, E., Chapman, MW, Morbidity at bone graft donor sites. *J Orthop Trauma* **1989**, *3* (3), 4.
- 4. Jang, J.-H.; Castano, O.; Kim, H.-W., Electrospun materials as potential platforms for bone tissue engineering. *Advanced Drug Delivery Reviews* **2009**, *61* (12), 1065-1083.
- 5. Liang, D.; Hsiao, B. S.; Chu, B., Functional electrospun nanofibrous scaffolds for biomedical applications. *Adv. Drug Del. Rev.* **2007**, *59* (14), 1392-1412.
- 6. Miszuk, J. M.; Xu, T.; Yao, Q.; Fang, F.; Childs, J. D.; Hong, Z.; Tao, J.; Fong, H.; Sun, H., Functionalization of PCL-3D electrospun nanofibrous scaffolds for improved BMP2-induced bone formation. *Applied materials today* **2018**, *10*, 194-202.
- 7. Weiner, S.; Wagner, H. D., The material bone: structure-mechanical function relations. *Annu. Rev. Mater. Sci.* **1998**, *28* (1), 271-298.
- 8. Reznikov, N.; Shahar, R.; Weiner, S., Bone hierarchical structure in three dimensions. *Acta Biomaterialia* **2014**, *10* (9), 3815-3826.
- 9. Frohbergh, M. E.; Katsman, A.; Botta, G. R.; Lazarovici, P.; Schauer, C. L.; Wegst, U. G. K.; Lelkes, P. I., Electrospun hydroxyapatite-containing chitosan nanofibers crosslinked with genipin for bone tissue engineering. *Biomaterials* **2012**, *33* (36), 9167-9178.
- 10. Doustgani, A.; Vasheghani-Farahani, E.; Soleimani, M.; Hashemi-Najafabadi, S., Optimizing the mechanical properties of electrospun polycaprolactone and nanohydroxyapatite composite nanofibers. *Composites Part B-Engineering* **2012**, *43* (4), 1830-1836.

- 11. Jose, M. V.; Thomas, V.; Xu, Y. Y.; Bellis, S.; Nyairo, E.; Dean, D., Aligned bioactive multi-component nanofibrous nanocomposite scaffolds for bone tissue engineering. *Macromolecular Bioscience* **2010**, *10* (4), 433-444.
- 12. Talham, D. R., Biomineralization: Principles and Concepts in Bioinorganic Materials Chemistry Stephen Mann. Oxford University Press, New York, 2001. *Crystal Growth & Design* **2002**, *2* (6), 675-675.
- 13. Luickx, N.; Van den Vreken, N.; Segaert, J.; Declercq, H.; Cornelissen, M.; Verbeeck, R., Optimization of the time efficient calcium phosphate coating on electrospun poly(d,l-lactide). *Journal of Biomedical Materials Research Part A* **2015**, *103* (8), 2720-2730.
- 14. Hadisi, Z.; Nourmohammadi, J.; Mohammadi, J., Composite of porous starch-silk fibroin nanofiber-calcium phosphate for bone regeneration. *Ceramics International* **2015**, *41* (9), 10745-10754.
- 15. Jaiswal, A. K.; Kadam, S. S.; Soni, V. P.; Bellare, J. R., Improved functionalization of electrospun PLLA/gelatin scaffold by alternate soaking method for bone tissue engineering. *Applied Surface Science* **2013**, *268*, 477-488.
- 16. Hartgerink, J. D.; Beniash, E.; Stupp, S. I., Self-assembly and mineralization of peptide-amphiphile nanofibers. *Science* **2001**, *294* (5547), 1684-1688.
- 17. Zhang, X.; Li, Z. Y.; Zhu, X. X., Biomimetic mineralization induced by fibrils of polymers derived from a bile acid. *Biomacromolecules* **2008**, *9* (9), 2309-2314.
- 18. Tampieri, A.; Celotti, G.; Landi, E.; Sandri, M.; Roveri, N.; Falini, G., Biologically inspired synthesis of bone-like composite: Self-assembled collagen fibers/hydroxyapatite nanocrystals. *Journal of Biomedical Materials Research Part A* **2003**, *67A* (2), 618-625.
- 19. Falini, C.; Fermani, S.; Ripamonti, A., Oriented crystallization of octacalcium phosphate into beta-chitin scaffold. *Journal of Inorganic Biochemistry* **2001**, *84* (3-4), 255-258.
- 20. Liu, Y.; Kim, Y. K.; Dai, L.; Li, N.; Khan, S. O.; Pashley, D. H.; Tay, F. R., Hierarchical and non-hierarchical mineralisation of collagen. *Biomaterials* **2011**, *32* (5), 1291-1300.
- 21. Yu, S.-H.; Cölfen, H.; Tauer, K.; Antonietti, M., Tectonic arrangement of BaCO3 nanocrystals into helices induced by a racemic block copolymer. *Nat. Mater.* **2005**, *4* (1), 51-55.
- 22. Tjandra, W., Yao, J, Ravi, P, Tam, KC, Alamsjah, A, Nanotemplating of calcium phosphate using a double-hydrophilic block Copolymer. *Chem. Mater.* **2005**, *17*, 8.
- 23. Lee, J. H.; Shofner, M. L., Copolymer-mediated synthesis of hydroxyapatite nanoparticles in an organic solvent. *Langmuir* **2013**, *29* (34), 10940-4.
- 24. Kim, Y.-Y.; Fielding, L. A.; Kulak, A. N.; Nahi, O.; Mercer, W.; Jones, E. R.; Armes, S. P.; Meldrum, F. C., Influence of the Structure of Block Copolymer Nanoparticles on the Growth of Calcium Carbonate. *Chem. Mater.* **2018**, *30* (20), 7091-7099.
- 25. Rajasekharan, A. K.; Andersson, M., Role of nanoscale confinement on calcium phosphate formation at high supersaturation. *Crystal Growth & Design* **2015**, *15* (6), 2775-2780.
- 26. Song, R. Q.; Hoheisel, T. N.; Sai, H.; Li, Z.; Carloni, J. D.; Wang, S.; Youngman, R. E.; Baker, S. P.; Gruner, S. M.; Wiesner, U.; Estroff, L. A., Formation of periodically-ordered calcium phosphate nanostructures by block copolymer-directed self-assembly. *Chemistry of Materials* **2016**, *28* (3), 838-847.
- 27. Chen, X.; Gleeson, S. E.; Yu, T.; Khan, N.; Yucha, R. W.; Marcolongo, M.; Li, C. Y., Hierarchically ordered polymer nanofiber shish kebabs as a bone scaffold material. *J Biomed Mater Res A* **2017**, *105* (6), 1786-1798.

- 28. Chen, X.; Wang, W.; Cheng, S.; Dong, B.; Li, C. Y., Mimicking bone nanostructure by combining block copolymer self-assembly and 1D crystal nucleation. *ACS Nano* **2013**, *7* (9), 8251-7.
- 29. Gleeson, S. E.; Kim, S.; Yu, T.; Marcolongo, M.; Li, C. Y., Size-dependent soft epitaxial crystallization in the formation of blend nanofiber shish kebabs. *Polymer* **2020**, *202*, 122644.
- 30. Yu, T.; Gleeson, S. E.; Li, C. Y.; Marcolongo, M., Electrospun poly(\(\varepsilon\)-caprolactone) nanofiber shish kebabs mimic mineralized bony surface features. *Journal of Biomedical Materials Research Part B: Applied Biomaterials* **2019**, *107* (4), 1141-1149.
- 31. Wang, B.; Li, B.; Xiong, J.; Li, C. Y., Hierarchically ordered polymer nanofibers via electrospinning and controlled polymer crystallization. *Macromolecules* **2008**, *41* (24), 9516-9521.
- 32. Chen, X., Dong, B, Wang, B, Shah, R, Li, CY, Crystalline block copolymer decorated, hierarchically ordered polymer nanofibers. *Macromol* **2010**, *43* (23), 10.
- 33. Attia, A. C.; Yu, T.; Gleeson, S. E.; Petrovic, M.; Li, C. Y.; Marcolongo, M., A review of nanofiber shish kebabs and their potential in creating effective biomimetic bone scaffolds. *Regenerative Engineering and Translational Medicine* **2018**, *4* (3), 107-119.
- 34. Li, L.; Li, C. Y.; Ni, C., Polymer crystallization-driven, periodic patterning on carbon nanotubes. *J. Am. Chem. Soc.* **2006**, *128* (5), 1692-9.
- 35. Xie, Q.; Chang, X.; Qian, Q.; Pan, P.; Li, C. Y., Structure and morphology of poly (lactic acid) stereocomplex nanofiber shish kebabs. *ACS Macro Letters* **2020**, *9*, 103-107.
- 36. Jing, X., Mi, H, Wang, X, Peng, X, Turng, L, Shish-Kebab-Structured Poly(ε-Caprolactone) Nanofibers Hierarchically Decorated with Chitosan-Poly(ε-Caprolactone) Copolymers for Bone Tissue Engineering *ACS Appl Mater Interfaces* **2015**, *7*, 11.
- 37. Jing, X.; Jin, E.; Mi, H. Y.; Li, W. J.; Peng, X. F.; Turng, L. S., Hierarchically decorated electrospun poly(epsilon-caprolactone)/nanohydroxyapatite composite nanofibers for bone tissue engineering. *Journal of Materials Science* **2015**, *50* (12), 4174-4186.
- 38. Kokubo, T.; Takadama, H., How useful is SBF in predicting in vivo bone bioactivity? *Biomaterials* **2006**, *27* (15), 2907-2915.
- 39. Tas, A. C., The use of physiological solutions or media in calcium phosphate synthesis and processing. *Acta Biomaterialia* **2014**, *10* (5), 1771-1792.
- 40. BarrÈre, F.; Layrolle, P.; van Blitterswijk, C. A.; de Groot, K., Biomimetic calcium phosphate coatings on Ti6Al4V: a crystal growth study of octacalcium phosphate and inhibition by Mg2+ and HCO3-. *Bone* **1999**, *25* (2, Supplement 1), 107S-111S.
- 41. Shin, K.; Jayasuriya, A. C.; Kohn, D. H., Effect of ionic activity products on the structure and composition of mineral self assembled on three-dimensional poly(lactide-co-glycolide) scaffolds. *Journal of biomedical materials research*. *Part A* **2007**, *83* (4), 1076-1086.
- 42. Meng, Z. X.; Li, H. F.; Sun, Z. Z.; Zheng, W.; Zheng, Y. F., Fabrication of mineralized electrospun PLGA and PLGA/gelatin nanofibers and their potential in bone tissue engineering. *Materials Science & Engineering C-Materials for Biological Applications* **2013**, *33* (2), 699-706.
- 43. Zheng, Y.; Dong, G.; He, L.; Wu, G.; Zheng, H.; Deng, C., In vitro study of calcium phosphate layers on hydroxyapatite ceramics surface mineralized in different solutions. *Ceramics International* **2016**, *42* (1, Part B), 1660-1665.
- 44. Petzetakis, N. D., A. P.; O', Reilly., R. K., Cylindrical micelles from the living crystallization-driven self-assembly of poly(lactide)-containing block copolymers. *Chem. Sci.* **2011**, *2*, 955-960.

- 45. Wang, X. F.; Gao, Y. H.; Xu, Y. Y.; Li, X. Y.; Jiang, J.; Hou, J. H.; Han, W. J.; Li, Q.; Shen, C. Y., A prerequisite of the poly(epsilon-caprolactone) self-induced nanohybrid shish-kebab structure formation: An ordered crystal lamellae orientation morphology of fibers. *Macromolecular Chemistry and Physics* **2017**, *218* (24), 1700414.
- 46. Qi, H.; Zhou, T.; Mei, S.; Chen, X.; Li, C. Y., Responsive Shape Change of Sub-5 nm Thin, Janus Polymer Nanoplates. *ACS Macro Lett.* **2016**, *5* (6), 651-655.
- 47. He, W.-N.; Xu, J.-T., Crystallization assisted self-assembly of semicrystalline block copolymers. *Prog. Polym. Sci.* **2012**, *37* (10), 1350-1400.
- 48. Mei, S.; Li, C. Y., Terraced and Smooth Gradient Polymer Brushes via a Polymer-Single-Crystal-Assisted-Grafting-To Method. *Angew. Chem. Int. Ed.* **2018**, *57*, 15758-15761.
- 49. Roman, B.; Bico, J., Elasto-capillarity: deforming an elastic structure with a liquid droplet. *J. Phys.: Condens. Matter* **2010**, *22* (49), 493101.
- 50. Zhou, T.; Qi, H.; Han, L.; Barbash, D.; Li, C. Y., Towards controlled polymer brushes via a self-assembly-assisted-grafting-to approach. *Nature Communications* **2016**, *7*, 11119.
- 51. Wang, W.; Qi, H.; Zhou, T.; Mei, S.; Han, L.; Higuchi, T.; Jinnai, H.; Li, C. Y., Highly robust crystalsome via directed polymer crystallization at curved liquid/liquid interface. *Nat. Commun.* **2016,** *7*, 10599.
- 52. Drouet, C., Apatite formation: Why it may not work as planned, and how to conclusively identify apatite compounds. *BioMed Research International* **2013**, *2013*, 490946.

TABLE OF CONTENT

